Enriched photoelectrocatalytic degradation and photoelectric performance of BiOI photoelectrode by coupling rGO

Huan Wang [a], Yinghua Liang [a,b,*], Li Liu [b], Jinshan Hu [b], Ping Wu [c], Wenquan Cui [b,*]

[a] School of Chemical Engineering and Technology, Hebei University of Technology, Tianjin 300130, PR China
[b] College of Chemical Engineering, Hebei Key Laboratory for Environment Photocatalytic and Electrocatalytic Materials, North China University of Science and Technology, Tangshan, Hebei 063009, PR China
[c] Department of Applied Physics, Tianjin Key Laboratory of Low Dimensional Materials Physics and Preparing Technology, Faculty of Science, Tianjin University, Tianjin 300072, PR China

ARTICLE INFO

ABSTRACT

Reduced graphene oxide (rGO) wrapped *n*-type BiOI hybrids for enhanced photoelectrocatalytic (PEC) degradation of organic pollutants is reported. The Scanning Electron Microscope (SEM) images showed that the rGO was homogeneously coated on the surface of BiOI, forming a core@shell structure. Raman spectra, Fourier transform infrared (FT-IR) spectra, and X-ray photoelectron spectroscopy (XPS) analyses showed that an intense interaction was formed between rGO and BiOI, which could highly promote the photo-generated charge transfer rate and photoelectric conversion efficiency. It was experimentally demonstrated that the degradation efficiency of organic pollutants for PEC process was 40.6% and 62.7% higher than that of photocatalytic (PC) and electrocatalytic (EC) processes, respectively. Further analyses indicated that the improvement in PEC degradation of organic pollutants benefited from: (1) a strong interaction and a wide range of conjugation were formed in the hybrid system; (2) negative shifts for the flat band potential in case of BiOI@rGO composites.

© 2017 Elsevier B.V. All rights reserved.

1. Introduction

Photoelectrocatalysis has exhibited a bright application prospect for PEC water splitting, degradation of pollutants and reduction of CO_2, which attracted considerable attention in the field of environmental science [1]. Recently, a lot of work is committed to investigate novel and efficient photoelectrode materials to improve photoelectric conversion performance for solar energy. The use of hybridized structures is an important strategy since it can combine the properties from each element, resulting in an enhanced overall efficiency [2,3]. Besides, the hybrids built can broaden the spectral range of light absorption and promote photo-excited charge separation, leading to improved energy efficiencies [4]. Tailoring of the hybrids is a key factor in improving the energy conversion efficiency. Among the various hybrids photoelectrode materials, the core@shell structured materials exhibited superior photoconersion efficiencies and outstanding PEC activities. The fabricated core@shell structures can not only maximi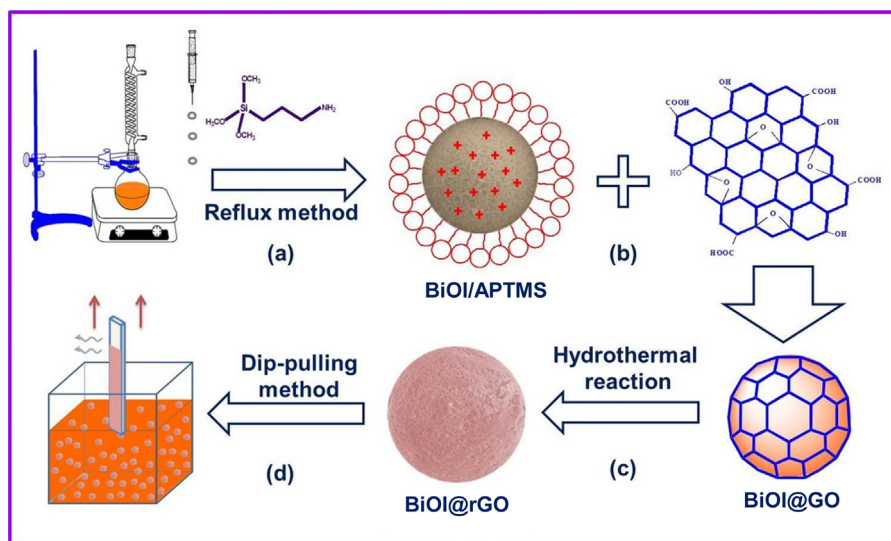ze the contact area and form effective hybridized effect (chemical interaction) on a large extent, but also protect the core materials from photocorrosion, thus effectively improving the photoelectric conversion efficiencies and stabilities.

Graphene, as a two-dimensional monolayer, is endowed with superior charge carrier mobility, high transparency, large surface area, flexible structure, and high thermal/chemical stability [5,6]. Fabrication of core@shell structured photoelectrodes with graphene as shell materials will promote the separation of photo-generated charge carriers and hinder the recombination of photo-excited electron-hole pairs due to the interactions between the large number of delocalized electrons in the π-conjugated structure and semiconductors [7–9]. Meanwhile, upon combination with graphene, the charge transfer efficiency at the interface of graphene and photoelectrodes can be highly accelerated; the separation of photo-generated charge carriers as well as the PEC performance can be effectively facilitated. It was reported that the core@shell structured hybrid such as graphene/TiO_2 [10,1], graphene-ZnO [11], and α-Fe_2O_3/graphene/$BiV_{1-x}Mo_xO_4$ [12] photoelectrodes showed excellent photoelectric conversion efficiencies and charge separation efficiencies for PEC degradation of organic pollutants and water splitting.

Recently, Bismuth oxyiodide (BiOI) with a narrow band gap of 1.7–1.9 eV has inspired great interest in pollutants degradation and

Scheme 1. Scheme for the preparation of BiOI@rGO photoelectrode. (a) Surface modification of BiOI, (b, c) fabrication of BiOI@GO and BiOI@rGO, (d) preparation of BiOI@rGO photoelectrode.

photoelectrochemical solar energy conversion due to its layered structure and more dispersive band characteristics compared with those transition metal oxides (TiO_2) [13–15]. Most researches about BiOI-based photoelectrode mainly focused on p-n heterostructures (BiOI/TiO_2 [16–18], BiOI-BiVO$_4$ [19], BiOI@ZnO [20], BiOI/BiOBr [21]), designed BiOI as a p-type of semiconductor, to improve the charge separation efficiencies of heterojunction photoelectrodes. Besides, n-type of BiOI semiconductors were also studied towards the photocatalytic water purification and photoelectrochemical properties due to the different preparation methods and non-stoichiometric composition, which exhibited strong photoconversion efficiencies and high photocatalytic activities. However, the number of researches about n-type of BiOI semiconductors toward photoelectrochemistry is relatively small. Hu et al. [22] synthesized n-type of BiOI photocatalyst by solvothermal method, which showed high photoelectric conversion efficiency and excellent visible light photocatalytic performance for oxidation of As (III) to As (V). Another n-type of BiOI micro-platelets, with the Photoelectrochemical Photocurrent Switching Effect [23] and a relatively higher anodic photocurrent than the cathodic photocurrent, were also prepared by a microwave assisted hydrothermal process [24]. In addition, Hahn et al. [15] fabricated n-type of BiOI nanoplatelet films, possessing incident photoconversion efficiency of over 20% and strong PEC performance as photoanodes in visible light range. However, the films showed poor stability in aqueous solutions because hydroxide layer was formed on the surface of photoelectrode that could inhibit the photo-induced charge transmission and result in suppressed PEC properties. These characteristics provide significant motivation for further study of n-type of BiOI photoelectrodes. Furthermore, it is highly important to find a modification method to protect the n-type of BiOI films and further improve the PEC performance for aqueous photoelectrochemistry.

Hence, for the first time, we report a core@shell structured BiOI@rGO hybrid photoelectrode in this study. The stability of n-type of BiOI photoelectrode can be highly improved to take advantage of the surface passivation of graphene. In addition, due to the π-conjugation in the structure of graphene and the hybridization between BiOI and rGO, the migration of interfacial charge carriers can be facilitated, the separation of photo-generated charges and photocatalytic quantum efficiency can be improved in an efficient manner, and thus significantly enhancing the PEC degradation of organic pollutants.

2. Experimental

2.1. Preparation of photoelectrode

All the reagents used were of analytical grade and were used without further purification. BiOI was synthesized by hydrothermal method. 0.9702 g of Bi(NO$_3$)$_3$·5H$_2$O and 0.3984 g of KI were dissolved separately in 30 mL ethylene glycol at room temperature for 30 min. The KI solution was added dropwise to the Bi(NO$_3$)$_3$ solution under magnetic stirring for 30 min. An orange-yellow suspension was obtained. Then, the resultant product was put into a 80 mL autoclave and maintained at 120 °C for 12 h. The collected BiOI crystals were washed with deionized water and dried at 80 °C for 10 h.

Graphene oxide (GO) was prepared by a modified Hummers method [25]. 3.0 g of graphite powder and 1.5 g of NaNO$_3$ were added to 70 mL of ice cold concentrated H$_2$SO$_4$ (98%). Then 9.0 g of KMnO$_4$ was gradually added to the above solution, while stirring and cooling continuously for 2.5 h and maintaining the temperature below 20 °C. The reaction was then heated to 35 °C and stirred for 3.5 h. Later, 150 mL of deionized water was slowly added to the reaction mixture. In order to increase the degree of oxidation of the GO product, the temperature of the bath was increased to 95 °C and the reaction was further allowed to continue for 1.5 h. This was followed by the addition of 30 mL of deionized water and 20 mL of 30% H$_2$O$_2$ aqueous solution, in succession. The obtained mixture was carefully washed with 250 mL of 10% HCl and centrifuged at 4000 r min^{-1} to remove the residual salts. Finally, the obtained GO product was purified by dialysis and centrifugation to remove any aggregates and other inorganic impurities. A dispersion of GO was obtained.

Preparation of BiOI@rGO: 0.4 g of BiOI was dispersed in 200 mL of absolute ethanol under sonication for 30 min. Then, 1 mL of 3-aminopropyl-trimethoxysilane (APTMS) was added and the mixture was refluxed at 80 °C for 4 h. After cooling to 25 °C, the collected product was washed with absolute ethanol several times to remove the residual APTMS. The APTMS-modified BiOI was then re-dispersed in 100 mL of absolute ethanol that contained different amount of negatively charged GO suspension (3.64 mg mL^{-1}) to obtained the weight ratios of GO to BiOI (BiOI@GO-0.5%, BiOI@GO-1.0%, BiOI@GO-2.0%, BiOI@GO-5.0%) under vigorous stirring for 30 min. The above suspension was then autoclaved in an auto-
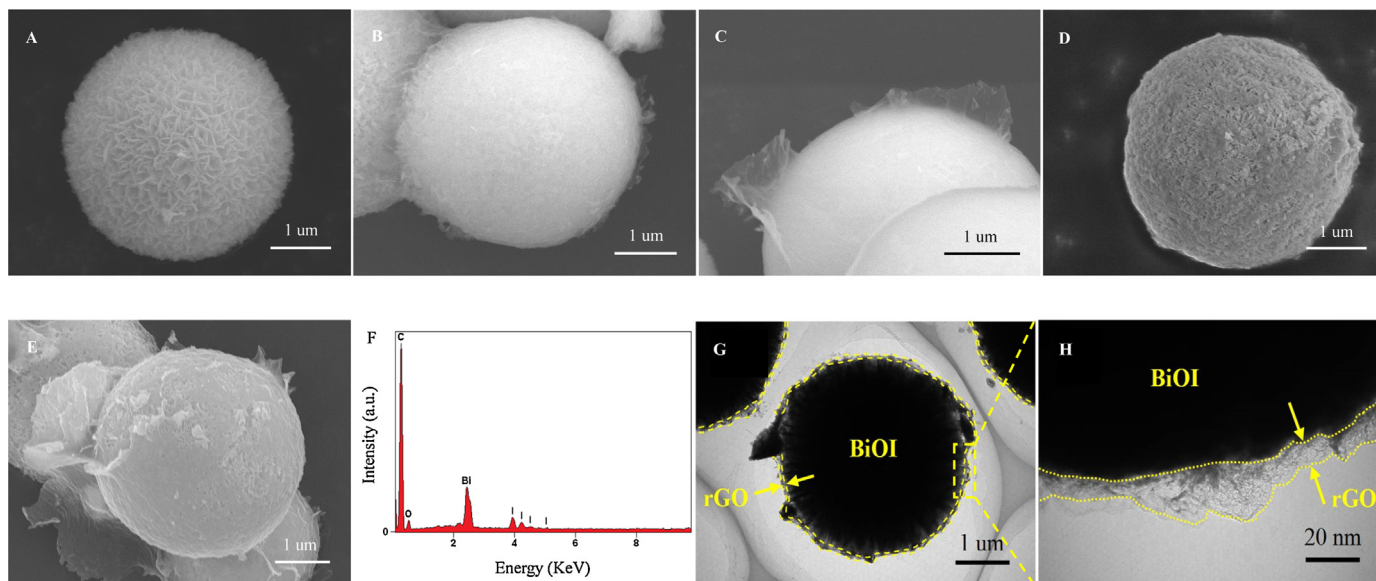
Fig. 1. SEM images of (A) BiOI, (B, C, D, E) BiOI@rGO-0.5%, BiOI@rGO-1.0%, BiOI@rGO-2.0%, BiOI@rGO-5.0%, (F) EDX spectra of BiOI@rGO-2.0%, (G, H) TEM images of BiOI@rGO-2.0%.
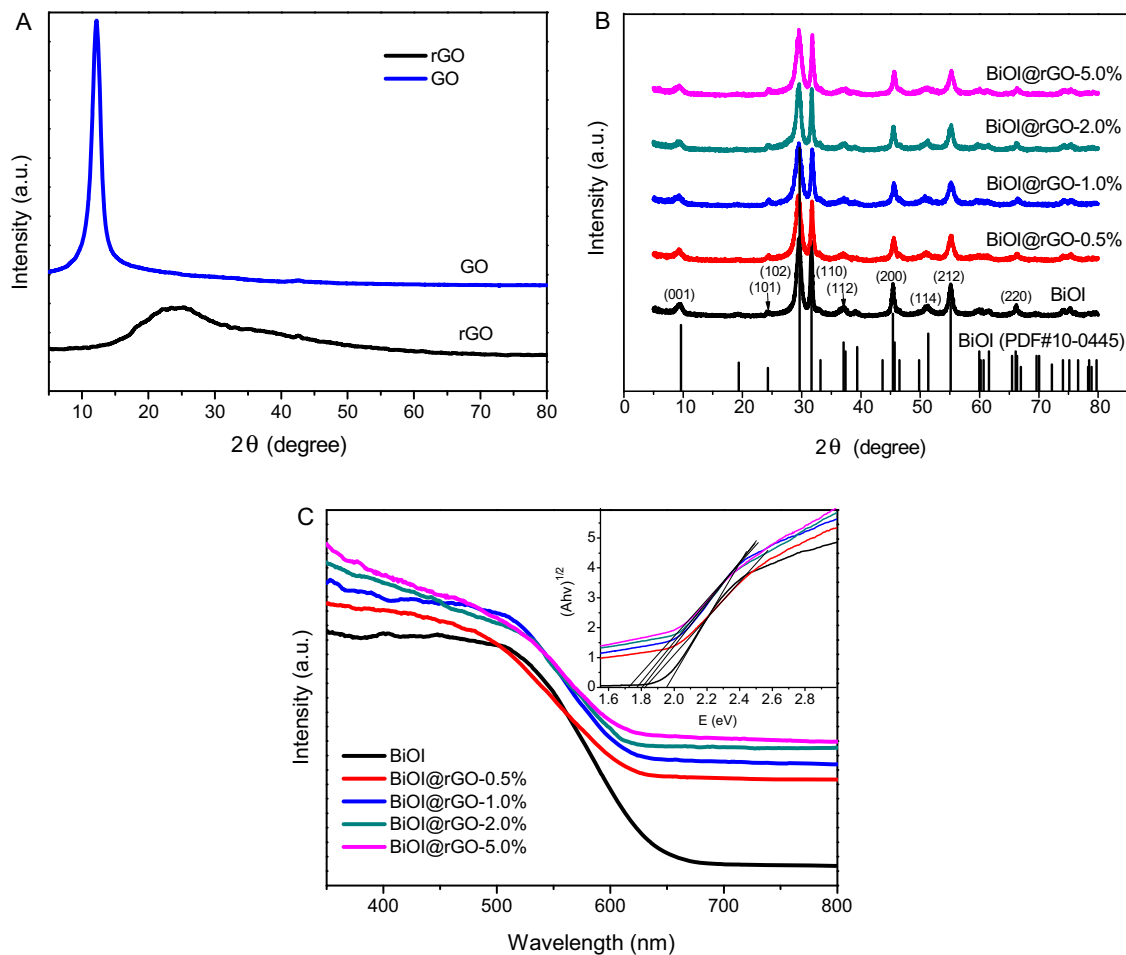

Fig. 2. (A, B) XRD patterns of the as-prepared samples, (C) UV–vis diffuse reflectance spectra of the composites. Inset: relationship of $(\alpha h\nu)^{1/2}$ versus E (eV).

clave at 120 °C for 2 h to reduce the GO to rGO. Finally, different weight ratios of rGO wrapped BiOI (BiOI@rGO-0.5%, BiOI@rGO-1.0%, BiOI@rGO-2.0%, BiOI@rGO-5.0%) were obtained.

Preparation of the photoelectrodes: To prepare the BiOI and BiOI@rGO hybrids photoelectrodes, BiOI and BiOI@rGO hybrids were dispersed in ethanol (5 mg mL^{-1}) by sonication to form a homogeneous suspension. Then the suspension was coated onto
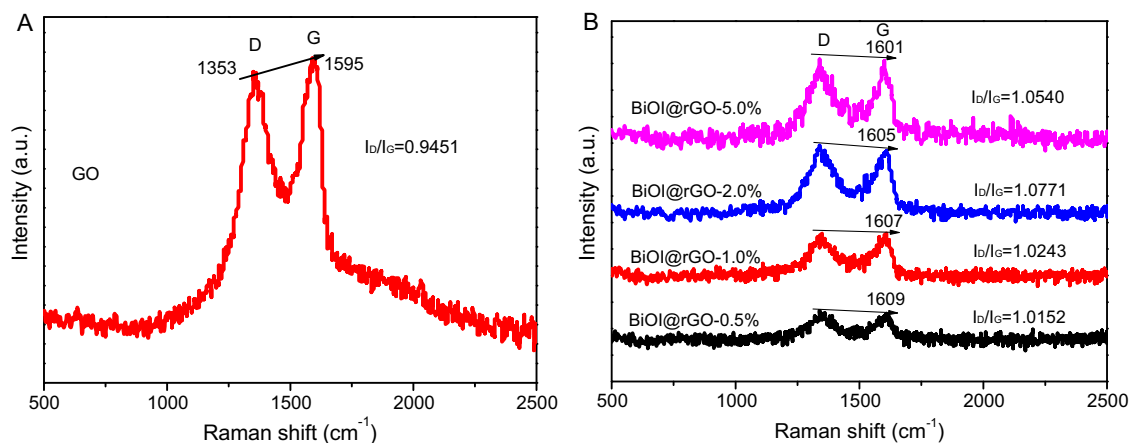
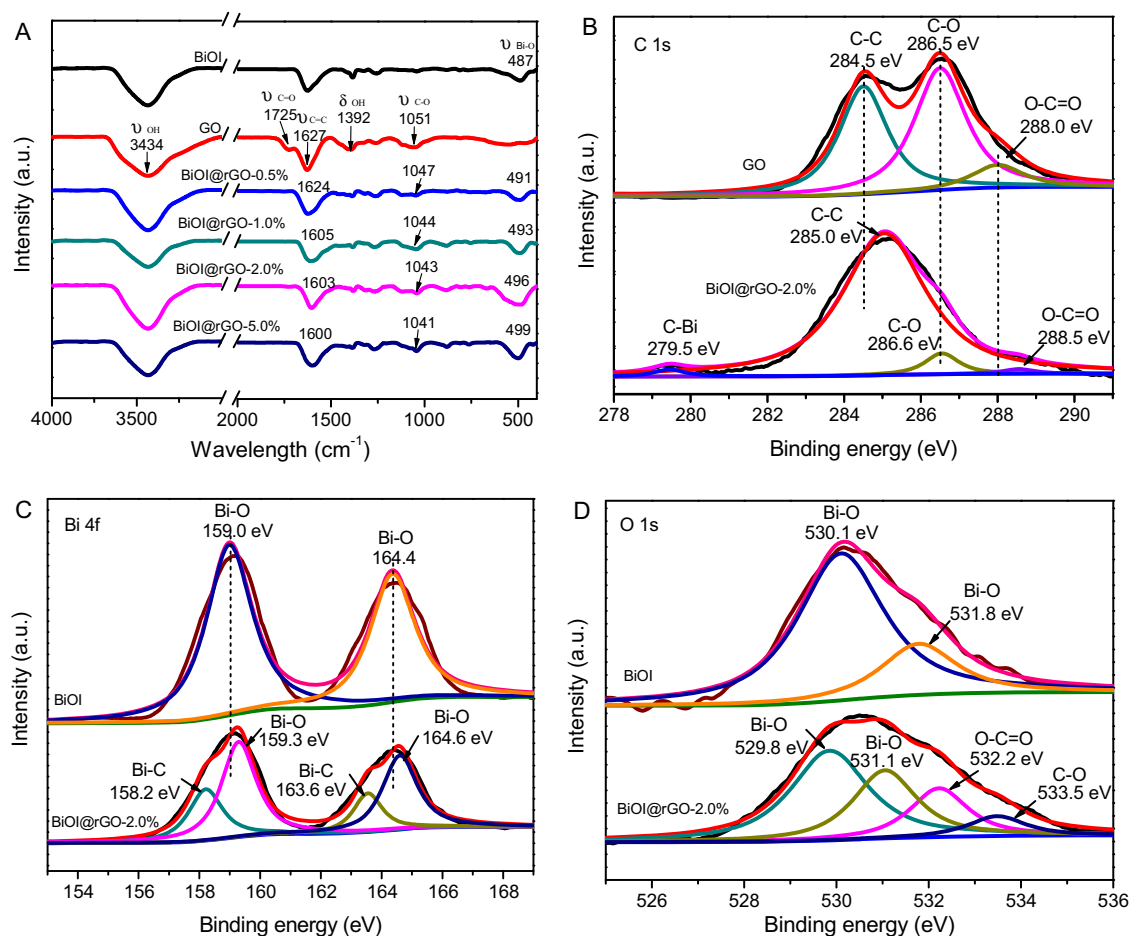**Fig. 3.** Raman spectra of GO (A) and BiOI@rGO hybrids (B).

Fig. 4. (A) FTIR spectra of BiOI, GO and BiOI@rGO hybrids, XPS spectra of C 1 s (B), Bi 4f (C), O 1 s (D) of the samples.

conducting indium tin oxide (ITO) glass by dip-pulling method so as to obtain about 3.0 mg cm^{-2} of the composite. Prior to dipping, the conducting ITO glass (4 cm × 2 cm) was cleaned ultrasonically and sequentially with deionized water, acetone, and absolute ethanol, for 30 min, and subsequently by nitrogen purging. After air drying, the as-prepared photoelectrode was calcined for 30 min at 350 °C under argon atmosphere to obtain the BiOI and BiOI@rGO hybrids photoelectrodes.

2.2. Characterization

The phase structures of the products were investigated by X-ray diffraction (XRD, Rigaku D/max-2500PC, Cu Kα radiation). The field scanning electron microscopy (SEM) equipped with an energy dispersive X-ray detector (EDX, Thermo NORAN system 7), and transmission electron microscopy (TEM) images were collected to study the morphologies of the resulting products. UV–vis absorption spectra were conducted on a Puxi UV1901 UV–vis spectrometer, using BaSO$_4$ as a reflectance reference. Raman spectra
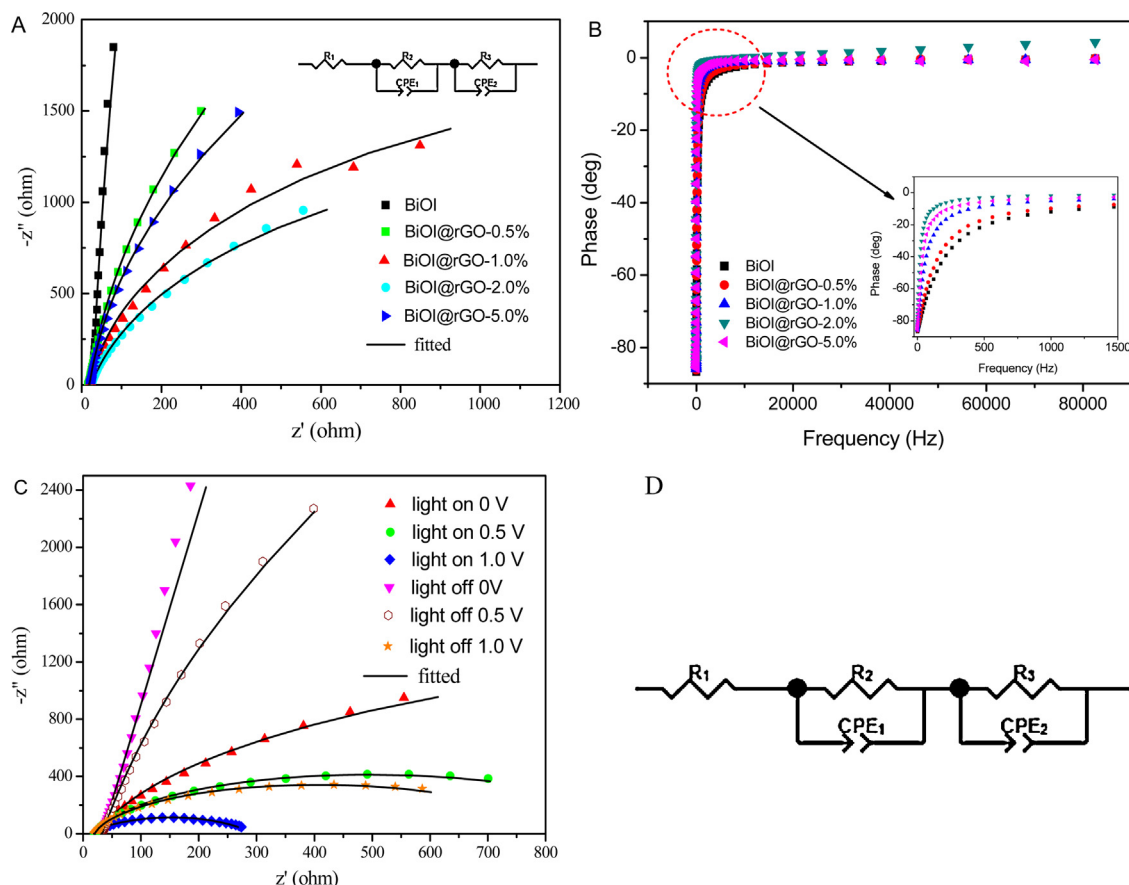
Fig. 5. (A) EIS plots of BiOI and BiOI@rGO hybrids under visible light, (B) Bode phase plots of BiOI and BiOI@rGO hybrids, (C) effects of photo-irradiation and bias potential on EIS of BiOI@rGO-2.0%, (D) the equivalent circuit of the devices.

were carried out on a microscopic confocal Raman spectrometer (Thermo DXR) by excitation using laser light (λ=514 nm). Fourier transform infrared (FT-IR) spectra were obtained by a Perkin Elmer System 2000 infrared spectrometer, using KBr as the reference sample. X-ray photoelectron spectroscopy (XPS) spectra were conducted on a Kratos Axis Ultra XPS system using monochromatic Al Kα radiation to study the surface states of the composites and their chemical shifts. The electron spin resonance (ESR) signals of spin-trapped radicals were recorded on a Bruker model ESR JEOL FA-200 spectrometer using spin-trap reagent DMPO (Sigma Chemical Co.) in water for hydroxyl radical and DMSO for superoxide radical, respectively.

2.3. Photoelectrochemical properties

Photoelectrochemical measurements were performed in a conventional three-electrode, single-compartment quartz cell on a CHI 660E Electrochemical Workstation. A 500 W Xe lamp purchased from Beijing Changtuo Co. Ltd., with a UV cut-off filter (420 nm) was used as the visible light source. A saturated calomel electrode (SCE) was used as the reference electrode and Pt as a counter electrode. 0.5 M Na$_2$SO$_4$ was used as electrolyte. The BiOI and BiOI@rGO hybrids photoelectrodes were used as the working electrodes. Electrochemical impedance spectroscopy (EIS) was performed at a 5 mV of alternating current signal in the frequency range of 1–10^5 Hz and the data obtained from the spectra were fitted using ZSimp-Win software. For all the photoelectrodes, a scan rate of 100 mV s^{-1} was used for the current versus (vs.) potential measurements (LSV). Photocurrent response was obtained from the potentiostatic measurements (current vs. time I-t) by illumination using visible light.

The Mott-Schottky plots were obtained at a frequency of 10 kHz to evaluate the flat band potentials (V$_{fb}$).

2.4. Photoelectrocatalytic degradation experiment

The PEC degradation experiments were performed in a 100 mL of three electrode quartz cell system with 500 W Xe lamp equipped with a UV cut-off filter (420 nm) on a CHI 660E Electrochemical Workstation. Cationic dye (RhB) was chosen as a model contaminant. The absorbance of RhB was measured at a wavelength of 554 nm. The initial concentration of RhB in the solution was 5 mg L^{-1}. 0.5 M Na$_2$SO$_4$ was used as electrolyte solution. Before irradiation, the system was kept in dark for 30 min to reach equilibrium of complete adsorption-deposition for each photoelectrode. The concentration of RhB was determined by a UV–vis spectrophotometry. Further intermediates and products were determined by HPLC–MS analysis with a UV detector at 550 nm. MS was performed using a Thermo Electron Corporation LTQ ion trap mass spectrometer equipped with an ESI source operated in positive or negative ion mode.

Besides, anionic dye (methyl orange, MO) and colorless organic pollutant (phenol) were also chosen as the model contaminants. The initial concentration of MO and phenol were 5 mg L^{-1}, 0.5 M Na$_2$SO$_4$ was used as electrolyte solution for the PEC degradation of MO. While 1.0 mmol L^{-1} Na$_2$SO$_4$ was used for the PEC degradation of phenol. The concentration of MO was determined by UV–vis spectrophotometry. As for phenol, it was determined by high performance liquid chromatography (HPLC).
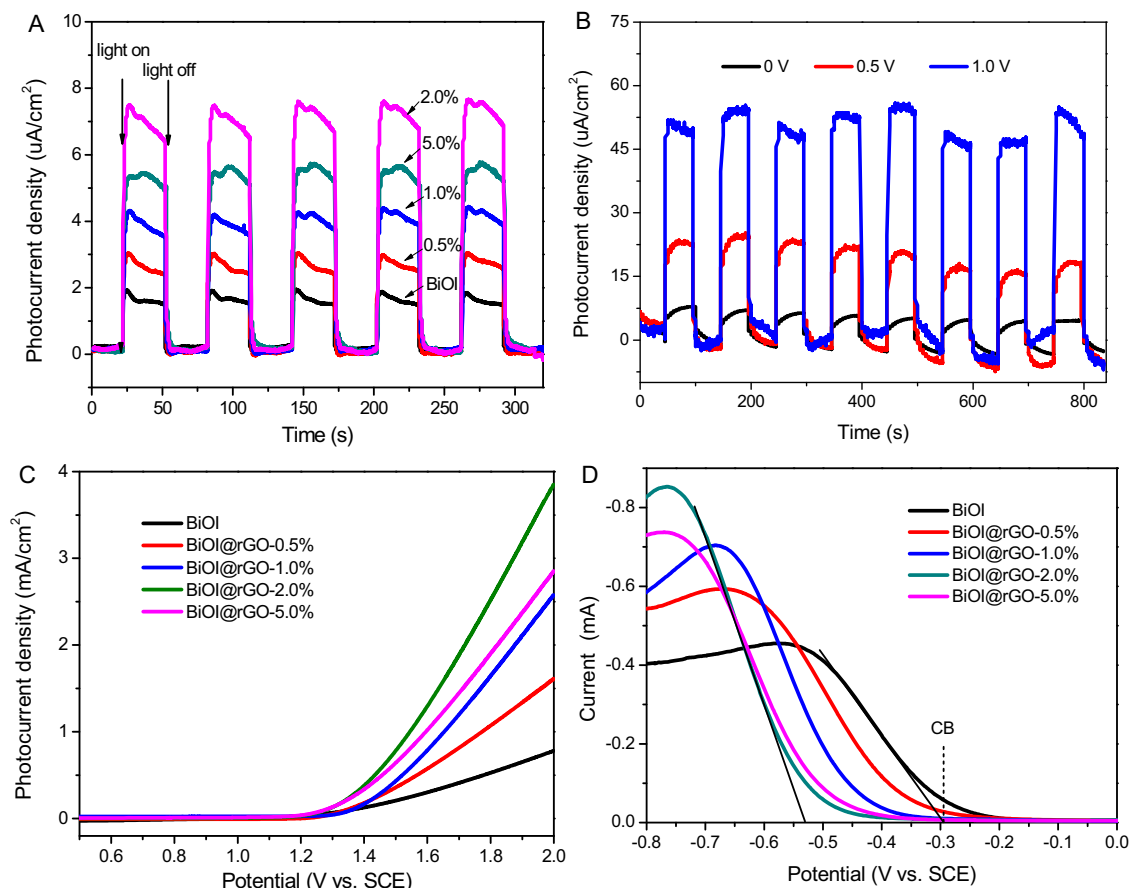
Fig. 6. (A) Transient photocurrent responses of photoelectrodes at 0.0 V (vs. SCE), (B) photocurrent responses of BiOI@rGO-2.0% photoelectrode at different bias potentials, (C) variation of photocurrent density vs. applied potential, (D) cathodic linear potential scan of the samples.

3. Result and discussion

3.1. Fabrication process of BiOI@rGO photoelectrode

The overall process for the fabrication of BiOI@rGO photoelectrode is shown in Scheme 1. (a) BiOI was positively charged by APTMS modification. (b) The BiOI@GO hybrid was fabricated through electrostatic interaction. (c) BiOI@rGO was prepared through hydrothermal treatment. (d) BiOI@rGO photoelectrode was synthesized by dip-pulling method on ITO.

3.2. Physical characterization of photoelectrodes

The morphologies, compositions and microstructures of the samples were obtained by SEM, EDX and TEM. Fig. 1A shows the uniform 3D hierarchical BiOI. The SEM images of BiOI@rGO with different weight ratios of rGO are shown in Fig. 1B–E. Obviously, BiOI microspheres were entirely wrapped by rGO in the weight ratios of 0.5%, 1.0%, 2.0% and 5.0%. The SEM images of BiOI@rGO hybrids with different rGO ratios under different magnifications are shown in Fig. S1. As shown, the thickness of the rGO layer increased with the increase of the rGO: BiOI weight ratio. Fig. 1G and H shows that rGO nano sheets are homogeneously anchored on the surface of BiOI with an average thickness of about 10 nm for BiOI@rGO-2.0%, which contributes to the increase in separation efficiency of photo-generated charges on BiOI surface and improved PEC quantum efficiency of the composites. Additionally, in the EDX spectra of BiOI@rGO-2.0% (Fig. 1F), C is attributed to rGO, whereas Bi, O and I are attributed to BiOI.

The phase purity and crystal structure of the obtained samples were examined by XRD. As shown in Fig. 2A, the sharp and intense peak at 2θ value of 12.2° is ascribed to (002) facet of GO. After GO was partially reduced, the characteristic diffraction peak of GO disappeared and a new peak appeared at 24°, indicating that rGO was formed [26]. The diffraction peaks of BiOI (Fig. 2B) are ascribed to tetragonal BiOI (JCPDS 10-0445). As for BiOI@rGO hybrids, rGO did not have influence on the lattice structure of BiOI. Moreover, no characteristic diffraction peaks of rGO were detected in BiOI@rGO, due to relatively low amounts of hybridization of rGO.

Optical characterization of BiOI@rGO hybrids was performed using UV–vis diffuse reflectance measurements (Fig. 2C). Compared with BiOI (Eg = 1.96 eV), as shown in the inset in Fig. 2C, red shifts are observed in visible light absorption edge for BiOI@rGO-0.5% (Eg = 1.83 eV), BiOI@rGO-1.0% (Eg = 1.81 eV), BiOI@rGO-2.0% (Eg = 1.77 eV) and BiOI@rGO-5.0% (Eg = 1.72 eV) hybrids. This phenomenon can be explained by the formation of a hybridized structure that can induce a direct chemical bond between C and Bi (formation of V-Bi) [27,2], and up-shift the valence band edge and thus reduce the band gap of BiOI [28,3]. Furthermore, formation of a hybridized structure between rGO and BiOI can effectively facilitate the migration efficiency of photo-induced charges, suppress the charge recombination, and thus improve the PEC performance.

Formation of the chemical bonding between rGO and BiOI was further investigated by Raman spectroscopy, FTIR, and XPS analysis. The Raman spectra of GO and BiOI@rGO hybrids are shown in Fig. 3. The typical features of graphene in Raman spectra are the D band at approximately 1353 cm^{-1} and the G band at around 1595 cm^{-1}. The D band reflects structural defects associated with introduction of oxygen containing functional groups to the graphitic layers, while
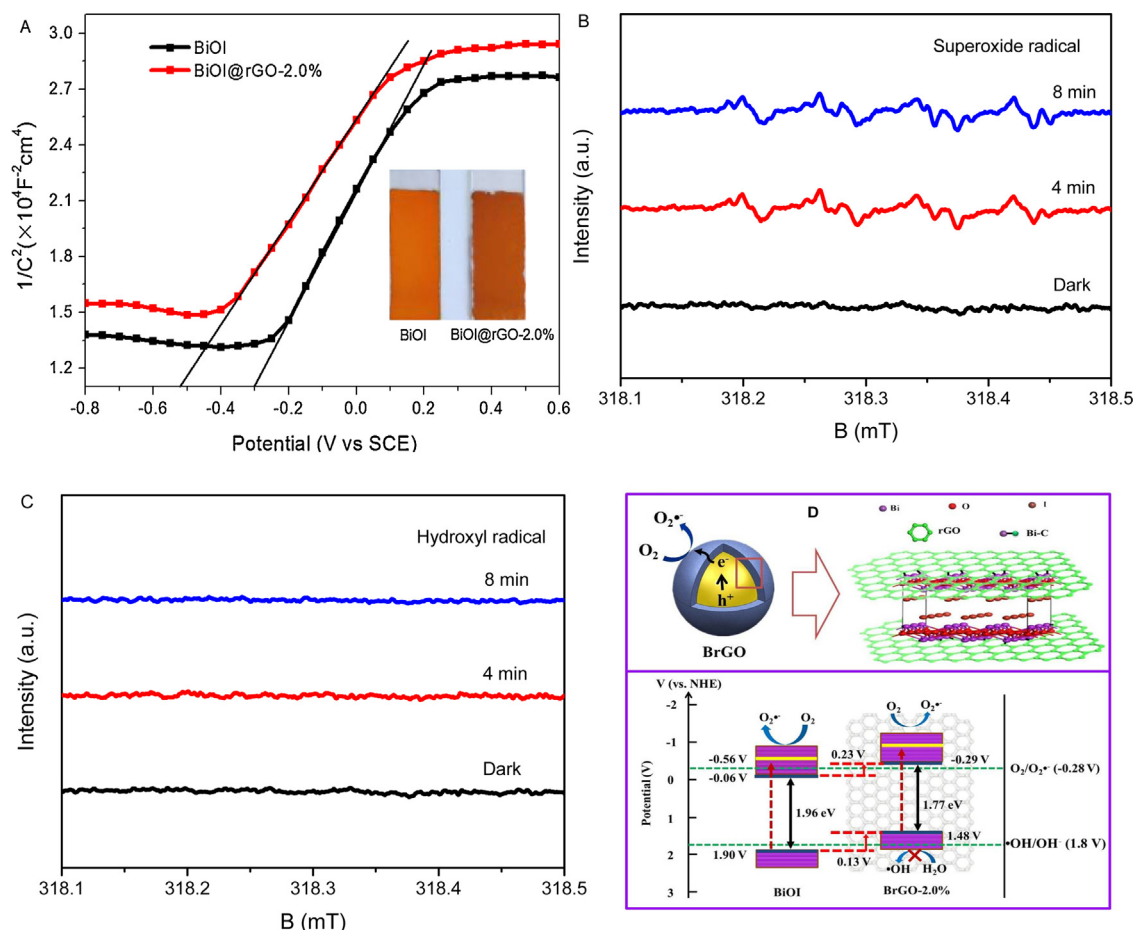
Fig. 7. (A) Mott-Schottky (MS) relationship for BiOI and BiOI@rGO-2.0%, DMPO spin-trapping ESR spectra of BiOI@rGO-2.0% in (B) DMSO and (C) water under visible light irradiation, (D) schematic diagrams of formation of BiOI@rGO-2.0% hybrid and corresponding proposed charge separation precess under visible light irradiation.

G band represents the symmetry and crystallinity of graphene. Compared with GO (Fig. 3A), the BiOI@rGO hybrids displayed increased peak intensity ratios (I_D/I_G) with the increasing rGO content (Fig. 3B), which suggests more defects and disorders in the graphitized structures, and considerable disruption of the symmetrical hexagonal graphitic lattice are formed for BiOI@rGO hybrids [29]. Besides, a band up-shift from $1595\,cm^{-1}$ to $1609\,cm^{-1}$ is observed for BiOI@rGO, compared with that of GO, indicating a change in the skeletal structure of graphene, and the formation of a strong chemical bond due to the hybridization between BiOI and rGO.

The FTIR spectra of BiOI, GO and BiOI@rGO hybrids are shown in Fig. 4A. The peak centered at $487\,cm^{-1}$ is ascribed to the stretching vibration of the Bi-O in BiOI [30]. The GO sample shows characteristic stretching vibrations of $C=O$ ($1725\,cm^{-1}$), $C=C$ ($1627\,cm^{-1}$), $C-O$ ($1051\,cm^{-1}$), and deformation vibration of $O-H$ ($1392\,cm^{-1}$) [7]. Obviously, with increasing the content of rGO in BiOI@rGO hybrids, the characteristic peaks of GO ($C=C$, $C-O$) shift to the lower frequency region, indicating that the $C=C$, $C-O$ bonds are weakened and a wide conjugated system is formed between rGO and BiOI. Similar phenomenon was also found in the case of ZnO hybridized monolayer polyaniline composite [31]. In addition, the stretching vibration of Bi-O ($487\,cm^{-1}$) for BiOI shifts to higher frequency region, due to the force constant values of Bi-O increase after BiOI is hybridized with rGO. The above phenomenon indicates that a strong chemical interaction between rGO and BiOI is formed, which is one of the key factors that can improve the PEC performance of BiOI@rGO.

XPS was further used to investigate the hybridized effects for BiOI@rGO. Fig. 4B shows the C 1 s XPS spectra of GO and BiOI@rGO-2.0%. Notably, the C 1 s spectra of GO can be divided into three peaks at 284.5 eV, 286.5 eV, and 288.0 eV, corresponding to carbon atoms in different functional groups: $C-H$, $C-C$, $C=C$ (sp^2 bonded carbon), $C-O$ (hydroxyl/epoxy), and $O-C=O$ (carboxyl) functional groups, respectively [32]. After reduction, the peaks centered at 286.6 eV and 288.5 eV decrease to a large degree. In addition, the C 1 s peaks of BiOI@rGO-2.0% shift slightly to higher binding energy values compared with GO, which suggests that an intense interfacial interaction is formed in BiOI@rGO. Moreover, an additional peak at 279.5 eV is observed for BiOI@rGO-2.0% hybrid, due to the C-Bi bonds [9]. In addition, the peaks of Bi $4f_{7/2}$ and Bi $4f_{5/2}$ for Bi-O bonds in BiOI@rGO-2.0% shift up by 0.3 eV and 0.2 eV (Fig. 4C) compared with BiOI, respectively. Besides, two peaks appeared at 158.2 eV and 163.6 eV ascribed to $C-Bi$ bonds are found in BiOI@rGO-2.0%, which is in accordance with the results for graphene/$Bi_2O_2CO_3$ [9]. Compared with BiOI, the observed O 1 s peaks ascribed to Bi-O bond for BiOI@rGO-2.0% shift to lower binding energy values of 529.8 eV and 531.1 eV (Fig. 4D). All the chemical shifts reveal that chemical interaction is formed between rGO and BiOI [33]. The peaks ascribed to 532.2 eV and 533.5 eV in BiOI@rGO-2.0% are assigned to $O-C=O$ and $C-O$ functional groups in rGO.

In brief, the effects of chemical bonding between rGO and BiOI are confirmed by Raman, FTIR, and XPS analyses, and a wide conjugated system is formed that can significantly facilitate the fast migration of photogenerated carriers and improve the PEC performance of BiOI@rGO hybrids.
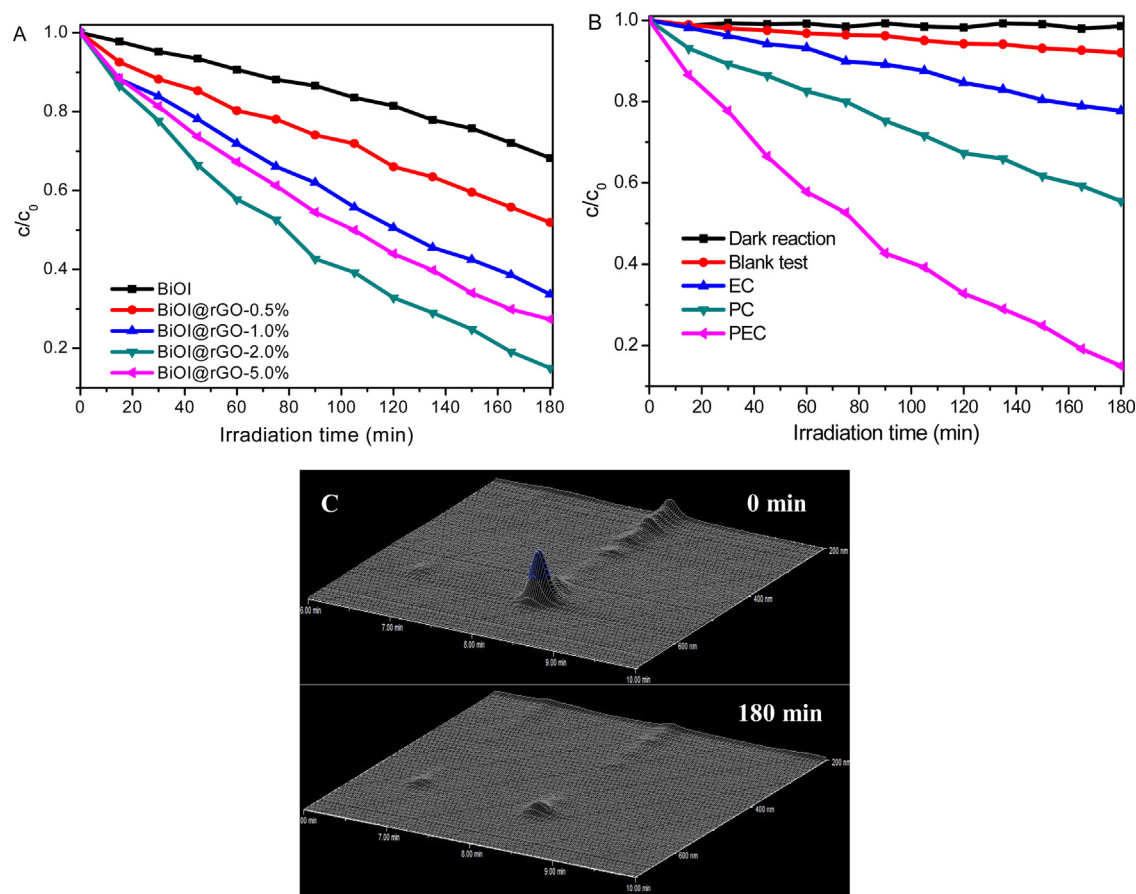
Fig. 8. (A) PEC degradation of RhB over BiOI and BiOI@rGO hybrids photoelectrodes at 1.0 V, (B) different degradation processes of RhB over BiOI@rGO-2.0% photoelectrode, (C) three-dimensional HPLC chromatographic spectra of RhB degradation (0 min and 180 min).

3.3. Photoelectrochemical performance measurements

To investigate the effect of rGO on the photoelectric properties of BiOI@rGO hybrids, series of photoelectrochemical measurements were used. The charge transfer property of the photoelectrode plays an important role in determining the PEC performance. Thus, Nyquist plots of EIS spectra of the photoelectrodes were measured. The semicircular Nyquist plots (Fig. 5A) indicate that the electron transfer at the interface of the electrodes plays a prominent role in the electrode process [34]. The equivalent circuit (Fig. 5D) of the devices was conducted to analyze the reaction mechanisms involved in the electrode process, in which R_1, R_2, R_3, and CPE represent the series resistance of the system, the resistance of semiconductor depletion layer, the charge transfer resistance in Helmholtz layer, and the chemical capacitance [35,4], respectively. The fitting results are shown in Table 1. The R_3 values of BiOI@rGO photoelectrodes decrease a lot compared with that of BiOI, in which the BiOI@rGO-2.0% photoelectrode gives the smallest R_3 value of 2.96×10^3 Ω, implying more efficient charge immigration and better conductivity for BiOI@rGO-2.0%. It is mainly due to the existence of rGO nanosheets in the core@shell structured BiOI@rGO hybrid that can serve as the framework to tightly hold the BiOI microsphere and the efficient channel (C-Bi bond) to transport charges, and thus give rise to greatly improved charge separation efficiency.

The Bode phase plots of BiOI and BiOI@rGO hybrids photoelectrodes are shown in Fig. 5B. The characteristic frequency peaks of BiOI@rGO hybrids shift to lower frequency than that of BiOI, in which BiOI@rGO-2.0% shows the lowest frequency of 68.40 Hz. The peak shifts reveal a more rapid electron transport process, because the frequency (f) is closely related to the lifetime (τ) of the injected electrons [33]:

$$\tau \approx 1/(2\pi f) \tag{1}$$

The calculated electron lifetimes of BiOI and BiOI@rGO hybrids are presented in Table 1. The electron lifetime of BiOI@rGO-2.0% (2.33 ms) is estimated 4.55 times higher than that of BiOI (0.42 ms), indicating a higher injected electron lifetime and greatly inhibited charge recombination in BiOI@rGO-2.0% photoelectrode.

The effects of photo-irradiation and applied bias on the EIS response of BiOI@rGO-2.0% photoelectrode were also investigated. It can be seen from Fig. 5C that the arc radius of EIS Nyquist plot can be decreased with visible light irradiation, and further decreased by the applied bias, which indicates that a large number of charge carriers are produced, and result in a higher PEC performance. The result further demonstrates that the applied bias can accelerate the PEC activity of BiOI@rGO hybrids.

The separation of photo-generated electron-hole pairs was further evaluated by measuring the transient photocurrent. Fig. 6A shows the photocurrent responses of BiOI and BiOI@rGO hybrids at 0.0 V under visible light. Obviously, the photocurrent densities of BiOI@rGO-0.5%, BiOI@rGO-1.0%, BiOI@rGO-2.0%, BiOI@rGO-5.0% hybrids are 2.64 uA cm⁻², 3.95 uA cm⁻², 7.18 uA cm⁻², and 5.59 uA cm⁻², which is 0.57 times, 1.35 times, 3.27 times, and 2.33 times higher than that of BiOI photoelectrode, respectively. The enhanced photocurrents can be ascribed to the superior charge mobility of graphene and the formation of C-Bi bond in BiOI@rGO hybrid [36]. In addition, when 0.5 V and 1.0 V bias are applied to the BiOI@rGO-2.0% hybrid photoelectrode (Fig. 6B), rapid and reversible photocurrent responses are obtained, and the photocur-
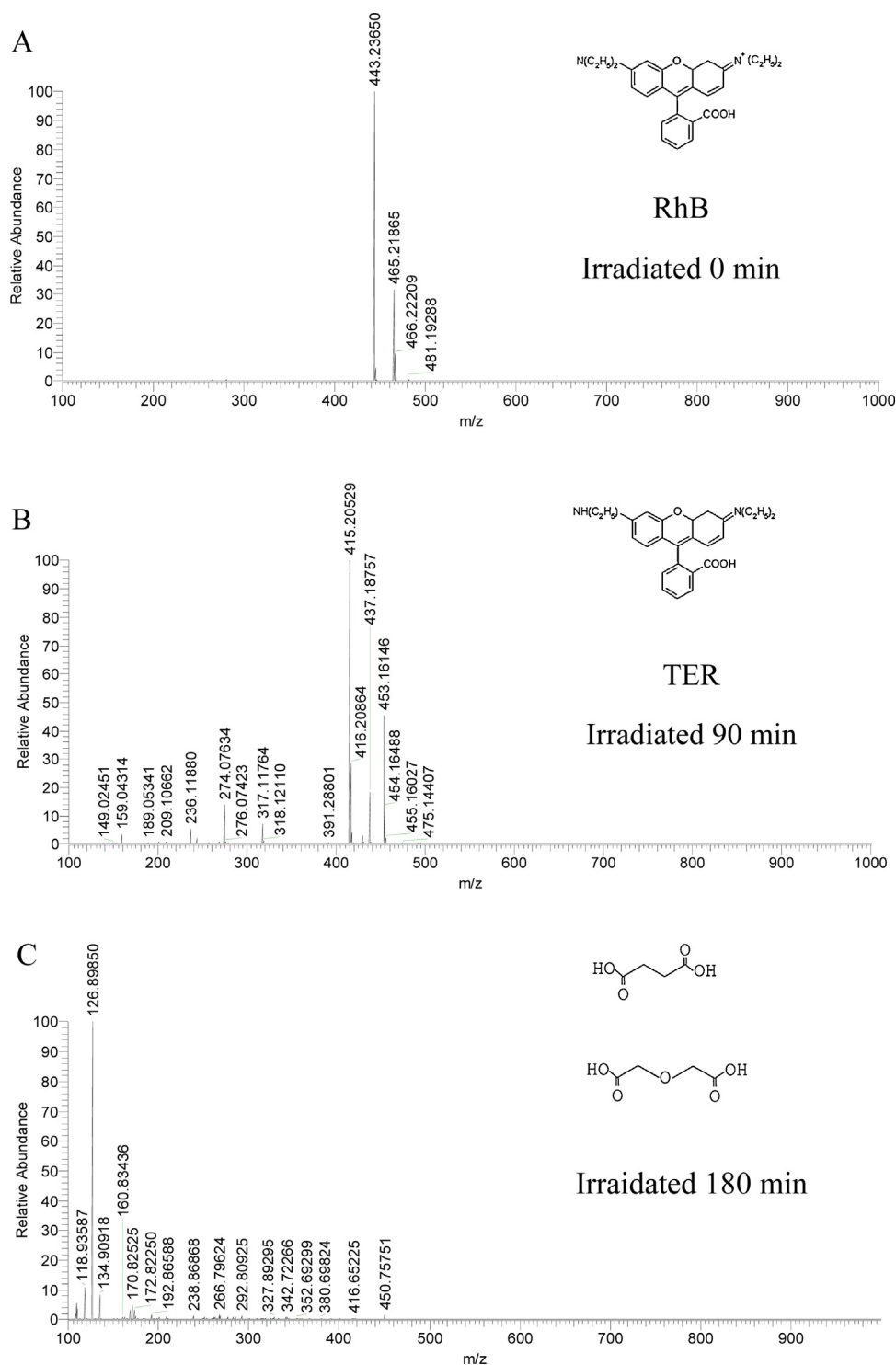
Fig. 9. HPLC–MS spectra detected during the PEC degradation of RhB over BiOI@rGO-2.0% photoelectrode at different irradiation time.

Table 1
EIS fitting data of BiOI and BiOI@rGO hybrids photoelectrodes.

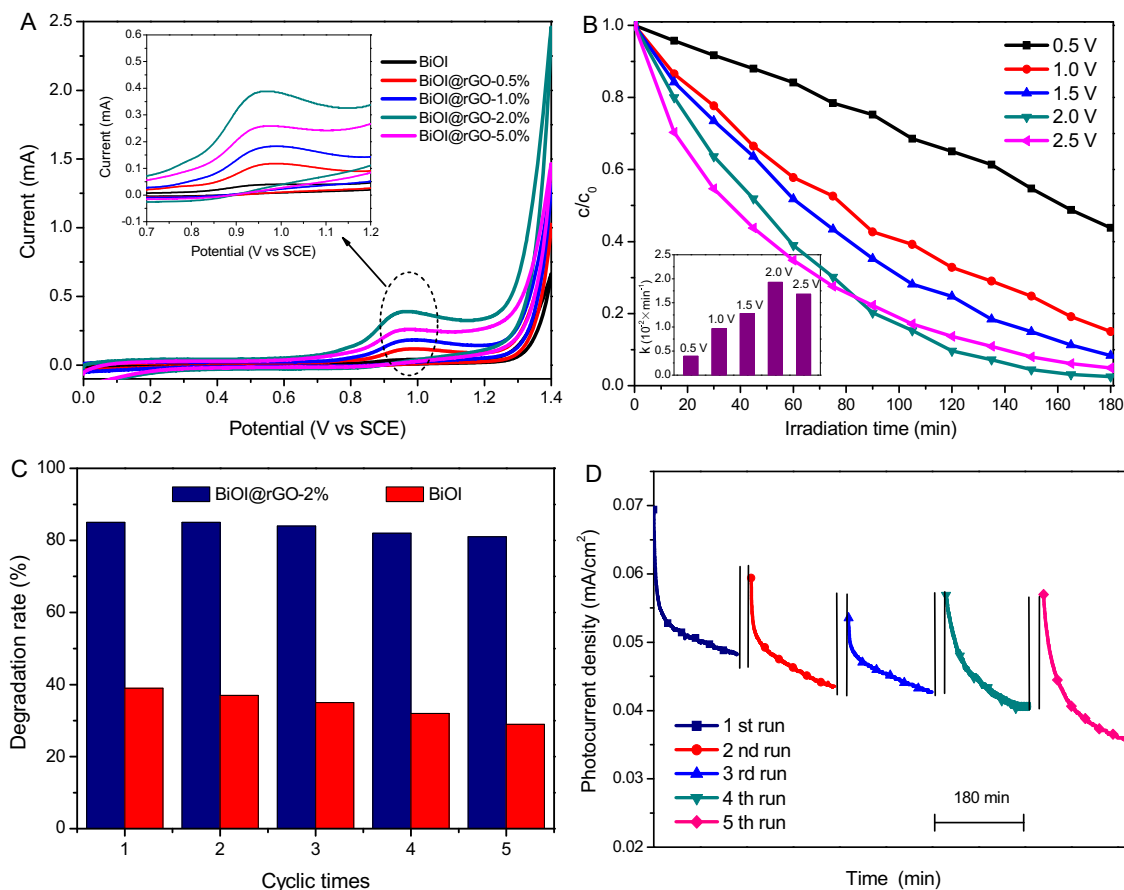| Photoelectrode	$R_1(\Omega)$	$R_2(\Omega)$	R_3 (Ω)	CPE_1 (F)	CPE_2 (F)	Electron lifetime (ms)
BiOI	21.42	6.62	1.81×10^5	8.74×10^{-5}	5.18×10^{-3}	0.42
BiOI@rGO-0.5%	16.60	6.47	1.22×10^4	1.10×10^{-4}	2.68×10^{-2}	0.62
BiOI@rGO-1.0%	21.10	1.94	1.22×10^4	9.37×10^{-2}	8.84×10^{-5}	0.90
BiOI@rGO-2.0%	21.81	1.21	2.96×10^3	2.66×10^{-5}	1.50×10^{-4}	2.33
BiOI@rGO-5.0%	17.63	3.70	8.18×10^3	7.87×10^{-3}	9.03×10^{-5}	1.31

Fig. 10. (A) cyclic voltammetry scans with BiOI and BiOI@rGO hybrids photoelectrodes in a 0.5 M Na_2SO_4 electrolyte with 5 mg/mL RhB, (B) comparison of the PEC degradation of RhB over BiOI@rGO-2.0% photoelectrode at various potentials, (C) cycling PEC degradation of RhB over BiOI@rGO-2.0%, and BiOI photoelectrodes at 1.0 V, (D) corresponding photocurrent densities of BiOI@rGO-2.0% during the cyclic experiments.

rent densities are reached from 7.18 $\mu A\,cm^{-2}$ to 52.85 $\mu A\,cm^{-2}$, with the increase of applied bias potentials. The PEC properties of BiOI and BiOI@rGO hybrid photoelectrodes are further studied by LSV measurement (Fig. 6C). Upon irradiation, the BiOI@rGO-2.0% photoelectrode exhibited a maximum photocurrent density of 3.85 $mA\,cm^{-2}$ at 2.0 V, which is about 4.07 times higher than that of BiOI. The enhancement of photocurrent density is ascribed to the effective electron collection and transportation characteristics of rGO nanosheets that can efficiently inhibit the recombination of photo-generated charges in BiOI@rGO hybrids [37]. Besides, negative shifts in the onset potential for the BiOI@rGO hybrids are observed compared with BiOI, indicating a smaller kinetic energy barrier for charge transfer across the interface of rGO and BiOI. Similarly, pervious researches also noticed negative shift in the onset potential for rGO modified Fe_2O_3 photoelectrode [38,39].

Moreover, understanding the effect of rGO on the band edge position of BiOI is also significant in investigating the improved PEC performance of BiOI@rGO hybrid. Therefore, cathodic linear scan measurements were performed to investigate the conduction band (CB) edge position of BiOI and BiOI@rGO hybrid [40]. The cathodic LSV curves of BiOI and BiOI@rGO hybrid are shown in Fig. 6D. It is apparent that the current increased abruptly, which is due to the formation of inversion layers that appeared at approximately −0.3 V (vs. SCE) for BiOI, that is assigned to the CB potential of BiOI. Obviously, the onset potentials (E_{CB}) of BiOI@rGO hybrid show negative shifts than that of pure BiOI, indicating a large accumulation of electrons at the interface of rGO and BiOI that reflect a suppressed charge carrier recombination, thus improving the overall efficiency of PEC degradation of organic pollutants. Sun et al. [41] also noticed

similar effects of graphene on graphene-Bi_2WO_6 photocatalyst in water splitting.

In order to confirm the semiconductor type of BiOI and the effect of rGO on the Fermi level of BiOI, Mott-Schottky (M-S) curves of BiOI and BiOI@rGO-2.0% hybrid are determined as shown in Fig. 7A. The slope of liner part of the curve in the M-S plot is positive, implying a n-type semiconductor for BiOI [42]. As shown in Fig. 7A, the CB potentials of BiOI and BiOI@rGO-2.0%, are found to be −0.30 V and −0.53 V vs. SCE (equivalent to −0.06 V and −0.29 V vs. NHE), respectively [43], which is in accordance with the results illustrated in Fig. 6D. Obviously, the conduction band potential of BiOI@rGO-2.0% shows a large negative shift of 0.23 V compared with that of BiOI. It is well known that the calculated work function of graphene is −4.42 eV vs. vacuum (equivalent to the Femi level (E_F) of graphene, −0.08 V vs. NHE) [44]. The E_F is not negative enough to cause the negative shift of E_F of BiOI@rGO. It can be inferred that the electronic interaction (C—Bi bond) in the core@shell interface of BiOI@rGO could cause a negative shift of the conduction band potential, resulting in a highly positioned conduction band and a stronger reductive power for the BiOI@rGO hybrid. Similar phenomenon of graphene on BiOBr [3] and Bi_2WO_6 [45] photocatalysts were also reported. The electron spin resonance (ESR) spectroscopy was performed to detect the existence of $\bullet O_2^-$. As shown in Fig. 7B, four apparent signals are observed under visible light irradiation, while no signal of $\bullet OH$ is observed (Fig. 7C), indicating that $\cdot OH$ oxidation is not the main reaction during the PEC process over BiOI@rGO-2.0% photoelectrode. The schematic diagrams of formation of C—Bi bond and proposed charge separation process in BiOI@rGO hybrid are shown in Fig. 7D. Under visible light irradiation, electrons in the
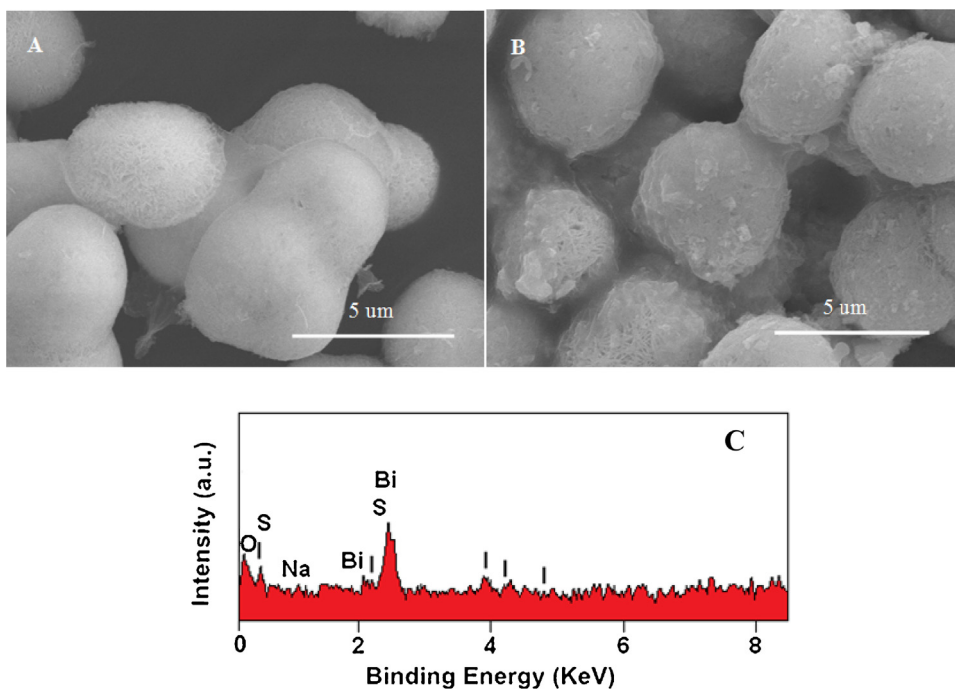
Fig. 11. SEM images of BiOI@rGO-2.0% electrode before (A) and after (B) PEC reaction, (C) EDX spectrum of the used BiOI@rGO-2.0% electrode.

valence band (VB) of BiOI could be excited up to a higher potential edge (-0.56 eV) after excitation to its CB [46]. In case of BiOI@rGO, the electrons in the VB of it can be further excited up to a more negative CB potential than that of the reformed CB edge potential of pure BiOI due to the hybridized effect in BiOI@rGO [47], and then flow to rGO to generate $\cdot O_2^-$. The holes left in the VB of BiOI and $\cdot O_2^-$ radicals are involved in the PEC process for the degradation of RhB.

3.4. Photoelectrocatalytic activities for photoelectrodes

To study the excellent PEC activity and stability of BiOI@rGO hybrid photoelectrodes, the PEC degradation of cationic dye (RhB) pollutant was evaluated under visible light irradiation (Fig. 8). The BiOI@rGO-2.0% photoelectrode exhibits the highest PEC degradation efficiency of 85.0% than that of BiOI and other BiOI@rGO hybrid photoelectrodes (Fig. 8A). However, when the rGO ratio increases to 5.0%, the PEC performance reduces. This is due to the fact that the thickness of rGO coated on the BiOI surface for BiOI@rGO-5.0% (Fig. S2) is about 20 nm to 30 nm, which is much higher than that of BiOI@rGO-2.0%. The excessive rGO can absorb some visible light and thus there exists a light harvesting competition between BiOI and rGO, resulting in a decreased PEC performance [48,49]. Compared with other degradation process, the PEC process of BiOI@rGO-2.0% shows 85.0% degradation of RhB (Fig. 8B), which is much higher than that of EC process (22.8%) and PC process (44.5%). In addition, it can be seen that the BiOI@rGO-2.0% photoelectrode exists hardly any adsorption capacity for RhB. In order to investigate the PEC degradation process of over BiOI@rGO-2.0% photoelectrode, the absorption spectra of RhB under visible light was studied (Fig. S3). As shown, the characteristic absorption peaks of RhB at 554 nm show hardly any shifts during the PEC degradation process over the BiOI@rGO-2.0% photoelectrode, indicating that mineralization of RhB dominates the PEC degradation process. Besides, HPLC–MS was used to investigate the degradation mechanism. Fig. 8C shows the three-dimensional HPLC chromatographic spectra of RhB degradation before and after the PEC degradation process. It can be seen that RhB is almost mineralized in 180 min,

which is in accordance with the results as shown in Fig. S3. The deethylation intermediates and other degradation products of RhB during the PEC process were monitored by (HPLC–MS). As shown in Fig. 9A–C, it can be concluded that the deethylation process of RhB is occurred within 90 min during the PEC process. Subsequently, the deethylation intermediates can be degraded to some open-ring organic compounds (such as adipic acid et al.), which are further mineralized to be CO_2 and H_2O by $\cdot O_2^-$ radical and holes [50].

The cyclic voltammetry scan of the BiOI and BiOI@rGO hybrid photoelectrodes in 0.5 M Na_2SO_4 solution with 5 mg mL^{-1} RhB is presented in Fig. 10A. The oxidation peak of RhB appears nearly 1.0 V, so the degradation of RhB will begin to perform by the combined electron-oxidation and photocatalysis simultaneously if the potential is above 1.0 V. Obviously, the BiOI@rGO hybrid photoelectrodes show much higher peak currents than that of pure BiOI at 1.0 V. The peak current of RhB oxidation is evaluated to be 0.39 mA for BiOI@rGO-2.0%, the highest oxidation peak current, suggesting an outstanding PEC performance for RhB degradation, which is in accordance with the resistance sequence in Fig. 5A. The above result indicates that the PEC activity toward RhB degradation of the BiOI photoelectrode can be effectively improved by the hybrid of rGO. The effect of bias potential on the PEC degradation of RhB was further studied (Fig. 10B), the PEC degradation efficiency of RhB increase with the increase of bias potential. It is notable that when the bias is above 1.5 V, the water molecules begin to be electrolyzed and produce some strong oxidizing substances ($\cdot OH$ radicals and O_2) on the surface of BiOI@rGO-2.0 photoelectrode [51]. These active substances can further oxidize the oxidation products of RhB. However, due to the competing reaction between H_2O decomposition and RhB degradation on the surface of BiOI@rGO-2.0% photoelectrode, the synergetic effect of PEC degradation efficiency decreases with the bias potential higher than 2.0 V. Similar result was also reported by Zhao et al. [52].

The photoelectrocatalytic stability of BiOI@rGO-2.0% photoelectrode was also evaluated by the cycling degradation experiments. As shown in Fig. 10C, the BiOI@rGO-2.0% photoelectrode still maintains above 80% with only 4.0% decrease for the degradation efficiency after used for 5 times, while the degradation efficiency
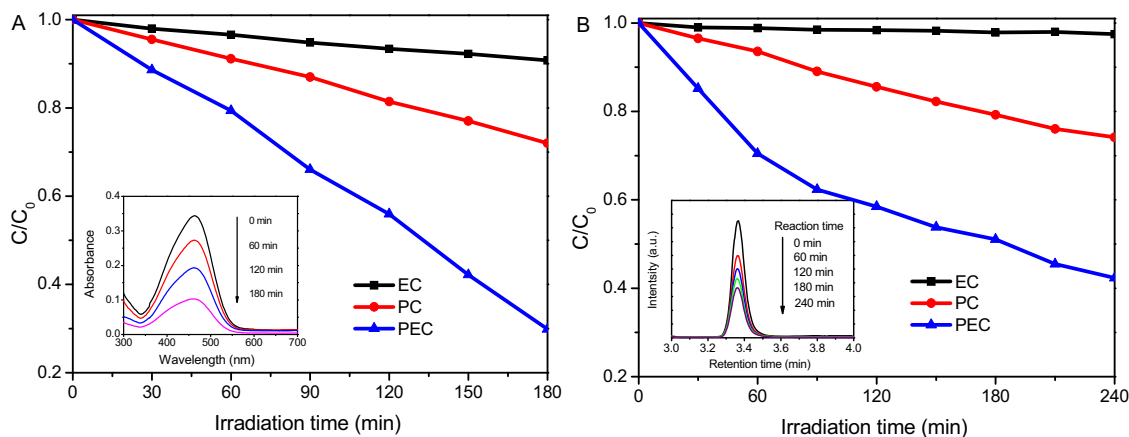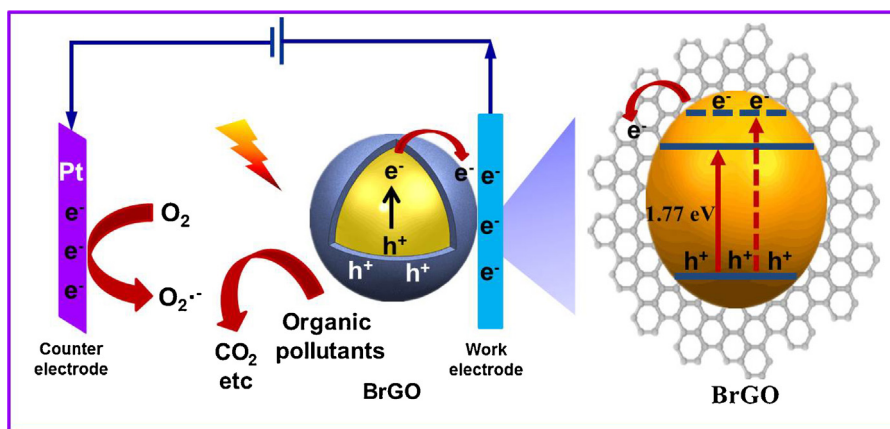
Fig. 12. Different degradation processes of MO (A) and phenol (B) over BiOI@rGO-2.0% photoelectrode.

Scheme 2. Schematic diagrams for the electron transfer in BiOI@rGO hybrid and the PEC degradation mechanism of RhB under visible light.

of pure BiOI photoelectrode decrease 10.0%. Meanwhile, the corresponding photocurrent densities of BiOI@rGO-2.0% photoelecrode during the cyclic experiments also exhibit well stabilities (Fig. 10D). In order to investigate the cause of the slightly decreased stability of the BiOI@rGO-2.0% photoelecrode, the high resolution SEM images of BiOI@rGO-2.0% photoelectrode before and after PEC reaction were performed and shown in Fig. 11A and B. Obviously, the BiOI@rGO-2.0% maintains a well core-shell structure after being used for five times. The EDX spectrum (Fig. 11C) of the used BiOI@rGO-2.0% indicates that some Na_2SO_4 electrolyte particles adsorb on the surface of the electrode, which may reduce the active cites and result in a slightly decreased PEC activity.

In order to confirm the extensive PEC degradation of organic pollutants for the as-prepared BiOI@rGO hybrid photoelectrode, the PEC degradation of anionic dye (methyl orange, MO) and colorless organic pollutant (phenol) measurements were also performed, as shown in Fig. 12A and B. The BiOI@rGO-2.0% shows a PEC degradation efficiency of 70.1% for MO in 180 min and a PEC degradation efficiency of 65.9% for phenol in 240 min under visible light irradiation, which are much higher than the EC and PC processes for MO and phenol degradation, indicating that the as-prepared BiOI@rGO hybrid photoelectrode possesses excellent PEC degradation of organic pollutants.

3.5. Proposed schematic mechanism

The proposed mechanism for PEC process in the BiOI@rGO photoelectrode is illustrated in Scheme 2. Under visible light irradiation, BiOI is excited. The photo-generated electrons are transferred to the surface of rGO due to a lower Femi level (−0.08 V vs. NHE) of rGO than the reformed CB edge potential of BiOI in BiOI@rGO hybrid, and subsequently flow to the collecting electrodes, leaving holes in the VB of BiOI. Thus, the electron-hole pairs are efficiently separated over the BiOI@rGO hybrid. The electrons on the counter electrode and the holes on the valence band of BiOI are involved in the PEC process for the degradation of RhB. As hybridized structure being established in the core@shell structure of BiOI@rGO, electrons injected from BiOI can quickly migrate to the collecting electrode through the presence of the large pool of delocalized electrons from its π-π graphitic carbon network, and leading to an improved PEC performance. Moreover, an external electric field further accelerates the transfer and separation of photo-induced charges, and this is also the reason for the improvement of the photocurrent upon the increase of the bias potential.

4. Conclusion

To summarize, a core@shell structured BiOI@rGO hybrid photoelectrode was proposed for highly efficient PEC degradation of organic pollutants. Graphene acted as the shell material can not only improve the poor stability of n-type of BiOI photoelectrode, but also enhance visible light absorption and combine with BiOI to form a hybrid structure to a large extent, resulting in a negatively shift flat band potential, and further improve the PEC degradation of organic pollutants.

Acknowledgements

Appendix A. Supplementary data

Supplementary data associated with this article can be found, in the online version, at http://dx.doi.org/10.1016/j.apcatb.2017.02.055.

References

[1] H.J. Zhang, G.H. Chen, D.W. Bahnemann, J. Mater. Chem. 19 (2009) 5089–5121.
[2] J. Su, X.X. Zou, G.D. Li, X. Wei, C. Yan, Y.N. Wang, J. Zhao, L.J. Zhou, J.S. Chen, J. Phys. Chem. C 115 (2011) 8064–8071.
[3] J.Z. Su, L.J. Guo, N.Z. Bao, C.A. Grimes, Nano Lett. 11 (2011) 1928–1933.
[4] A. Paracchino, V. Laporte, K. Sivula, M. Gratzel, E. Thimsen, Nat. Mater. 10 (2011) 456–461.
[5] A.K. Geim, K.S. Novoselov, Nat. Mater. 6 (2007) 183–191.
[6] S. Stankovich, D.A. Dikin, G.H.B. Dommett, K.M. Kohlhaas, E.J. Zimney, E.A. Stach, R.D. Piner, S.T. Nguyen, R.S. Ruoff, Nature 442 (2006) 282–286.
[7] X. Wei, C.M. Chen, S.Q. Guo, F. Guo, X.M. Li, X.X. Wang, H.T. Cui, L.F. Zhao, W. Li, J. Mater. Chem. A 2 (2014) 4667–4675.
[8] Q.J. Xiang, J.G. Yu, M. Jaroniec, Chem. Soc. Rev. 41 (2012) 782–796.
[9] Y.L. Zhang, D.Y. Li, Y.G. Zhang, X.F. Zhou, S.J. Guo, L.B. Yang, J. Mater. Chem. A 2 (2014) 8273–8280.
[10] H. Kim, G.-H. Moon, D. Monllor-Satoca, Y. Park, W. Choi, J. Phys. Chem. C 116 (2012) 1535–1543.
[11] Y.Y. Bu, Z.Y. Chen, W.B. Li, B.R. Hou, ACS Appl. Mater. Interfaces 5 (2013) 12361–12368.
[12] Y. Hou, F. Zuo, A. Dagg, P.Y. Feng, Nano Lett. 12 (2012) 6464–6473.
[13] K. Wang, F. Jia, Z. Zheng, L. Zhang, Electrochem. Commun. 12 (2010) 1764–1767.
[14] K. Zhao, X. Zhang, L. Zhang, Electrochem. Commun. 11 (2009) 612–615.
[15] N.T. Hahn, S. Hoang, J.L. Self, C. Buddie Mullins, ACS Nano 6 (2012) 7712–7722.
[16] G.P. Dai, J.G. Yu, G. Liu, J. Phys. Chem. C 115 (2011) 7339–7346.
[17] W.W. Zhao, S. Shan, Z.Y. Ma, L.N. Wan, J.J. Xu, H.Y. Chen, Anal. Chem. 85 (2013) 11686–11690.
[18] L.Y. Wang, W.A. Daoud, Appl. Surf. Sci. 324 (2015) 532–537.
[19] K.H. Ye, Z.S. Chai, J.W. Gu, X. Yu, C.X. Zhao, Y.M. Zhang, W.J. Mai, Nano Energy 18 (2015) 222–231.
[20] P.Y. Kuang, J.R. Ran, Z.Q. Liu, H.J. Wang, N. Li, Y.Z. Su, Y.G. Jin, S.Z. Qiao, Chem. Eur. J. 21 (2015) 15360–15368.
[21] H.L. Lin, H.F. Ye, X. Li, J. Cao, S.F. Chen, Ceram. Int. 40 (2014) 9743–9750.
[22] J. Hu, S.X. Weng, Z.Y. Zheng, Z.X. Pei, M.L. Huang, P. Liu, J. Hazard. Mater. 264 (2014) 293–302.
[23] M.E. Kazyrevich, M.V. Malashchonak, A.V. Mazanik, E.A. Streltsov, A.I. Kulak, C. Bhattacharya, Electrochim. Acta 190 (2016) 612–619.
[24] P. Kwoleka, K. Szaciłowski, Electrochim. Acta 104 (2013) 448–453.
[25] S. William, J.R. Hummers, R.E. Offeman, J. Am. Chem. Soc. 80 (1958), 1339–1339.
[26] J. Cheng, M. Zhang, G. Wu, X. Wang, J.H. Zhou, K.F. Cen, Environ. Sci. Technol. 48 (2014) 7076–7084.
[27] J.S. Lee, K.H. You, C.B. Park, Adv. Mater. 24 (2012) 1084–1088.
[28] M. Tu, S.L. Luo, G.X. Chen, J.H. Li, Chem. Eur. J. 18 (2012) 14359–14366.
[29] M.D. Ye, C. Chen, N. Zhang, X.R. Wen, W.X. Guo, C.J. Lin, Adv. Energy Mater. 4 (2014) 1301564.
[30] J. Cao, X. Li, H.L. Lin, S.F. Chen, X.L. Fu, J. Hazard. Mater. 239–240 (2012) 316–324.
[31] H. Zhang, R. Zong, Y. Zhu, J. Phys. Chem. C 113 (2009) 4605–4611.
[32] A.A. Dubale, W.N. Su, A.G. Tamirat, C.J. Pan, B.A. Aragaw, H.M. Chen, C.H. Chen, B.J. Hwang, J. Mater. Chem. A 2 (2014) 18383–18397.
[33] S.M. Sun, W.Z. Wang, L. Zhang, J. Phys. Chem. C 117 (2013) 9113–9120.
[34] H. Wang, L. Liu, Y.F. Wang, S.L. Lin, W.J. An, W.Q. Cui, Y.H. Liang, Mater. Lett. 160 (2015) 351–354.
[35] J. Xiang, Z.G. Liu, J.H. Ouyang, Y. Zhou, F.Y. Yan, Solid State Ionics 220 (2012) 7–11.
[36] Y.J. Wang, X.J. Bai, C.S. Pan, J. He, Y.F. Zhu, J. Mater. Chem. 22 (2012) 11568–11573.
[37] A.G. Tamirat, W.N. Su, A.A. Dubale, C.J. Pan, H.M. Chen, D.W. Ayele, J.F. Lee, B.J. Hwang, J. Power Sources 287 (2015) 119–128.
[38] F. Meng, J. Li, S.K. Cushing, J. Bright, M. Zhi, J.D. Rowley, Z. Hong, A. Manivannan, A.D. Bristow, N. Wu, ACS Catal. 3 (2013) 746–751.
[39] S. Rai, A. Ikram, S. Sahai, S. Dass, R. Shrivastav, V.R. Satsangi, RSC Adv. 4 (2014) 17671–17679.
[40] T.F. Yeh, F.F. Chan, C.T. Hsieh, H. Teng, J. Phys. Chem. C 115 (2011) 22587–22597.
[41] Z.H. Sun, J.J. Guo, S.M. Zhu, L. Mao, J. Ma, D. Zhang, Nanoscale 6 (2014) 2186–2193.
[42] J.T. Li, F.K. Meng, S. Suri, W.Q. Ding, F.Q. Huang, N.Q. Wu, Chem. Commun. 48 (2012) 8213–8215.
[43] A. Ishikawa, T. Takata, J.N. Kondo, M. Hara, H. Kobayashi, K. Domen, J. Am. Chem. Soc. 124 (2002) 13547–13553.
[44] K. Liu, Z. Hu, R. Xue, J. Zhang, J. Zhu, J. Power Sources 179 (2008) 858–862.
[45] E.P. Gao, W.Z. Wang, M. Shang, J.H. Xu, Phys. Chem. Chem. Phys. 13 (2011) 2887–2893.
[46] L.Z. Zhang, T.F. Zhang, D.J. Wang Xie, J. Phys. Chem. C 113 (2009) 7371–7378.
[47] J. Cao, B.Y. Xu, H.L. Lin, B.D. Luo, S.F. Chen, Chem. Eng. J. 185–186 (2012) 91–99.
[48] T.G. Xu, L.W. Zhang, H.Y. Cheng, Y.F. Zhu, Appl. Catal. B: Environ. 101 (2011) 382–387.
[49] J. Liu, L.K. Pan, Q.F. Zhao, T. Lv, G. Zhu, T.Q. Chen, T. Lu, Z. Sun, C.Q. Sun, Chem. Eng. J. 183 (2012) 238–243.
[50] Z. He, S.G. Yang, Y.M. Ju, C. Sun, J. Environ. Sci 21 (2009) 268–272.
[51] G.W. Muna, N. Tasheva, G.M. Swain, Environ. Sci. Technol. 38 (2004) 3674–3682.
[52] X. Zhao, Y.F. Zhu, Environ. Sci. Technol. 40 (2006) 3367–3372.